Turkish Journal of Electrical Engineering & Computer Sciences

http://journals.tubitak.gov.tr/elektrik/

Research Article

Turk J Elec Eng & Comp Sci
(2015) 23: 255 – 278

doi:10.3906/elk-1301-90

Control of oxygen excess ratio in a PEM fuel cell system using high-order sliding-mode controller and observer

Seyed Mehdi RAKHTALA[1,*], Abolfazl Ranjbar NOEI[1], Reza GHADERI[1], Elio USAI[2]

[1]Department of Electrical and Computer Engineering, Babol University of Technology, Babol, Iran
[2]Department of Electrical and Electronic Engineering, University of Cagliari, Cagliari, Italy

Received: 15.01.2013 • **Accepted:** 08.04.2013 • **Published Online:** 12.01.2015 • **Printed:** 09.02.2015

Abstract: The main objective of this manuscript is to design a high-order sliding-mode observer to provide finite time estimation of unmeasurable states (x_4: oxygen mass, x_5: nitrogen mass) together with the oxygen excess ratio (ratio of the input oxygen flow to the reacted oxygen flow in the cathode). This is done by applying second-order sliding modes through either super twisting or suboptimal controllers to control the proton exchange membrane fuel cell's breathing. The estimated oxygen excess ratio is controlled in a closed-loop system using 2 distinct sliding-mode approaches: a cascaded super twisting controller and a single-loop suboptimal structure. Simulation results are presented to make a quantitative comparison between the cascade and the single-loop configuration. The results verify that the cascade provides accurate reference tracking while the single-loop presents faster convergence.

Key words: Proton exchange membrane fuel cell, oxygen excess ratio, high-order sliding-mode observer, cascade control, second-order sliding mode

1. Introduction

A fuel cell is an electrochemical device to convert chemical energy into electrical energy with thermal dissipation [1]. In comparison with regular power resources, this offers several advantages, such as high efficiency and a flexible modular structure [2]. However, as a drawback, the reaction time constant is dominated by temperature and oxygen starvation during rapid load transients [3]. Therefore, the proton exchange membrane fuel cell (PEMFC) performance is closely related to the type of control system.

Oxygen starvation is a complicated phenomenon that causes a rapid decrease in the cell voltage, which creates hot spots in severe cases or even burns the surface of the membrane. Pukrushpan et al. [4,5] reported that acceptable amounts for the oxygen excess ratio (λ_{O2}) are within 2–2.4 based on the stack power. Therefore, it must be regulated around the constant value to cope with the oxygen starvation. This may be fulfilled through control of the oxygen-providing mechanism, i.e. the compressor PEMFC, to achieve a satisfactory performance. As a necessary condition, the dynamic response of the compressor motor controller has to be fast.

Recently, several control strategies were proposed for PEMFC systems. Among them, feedback linearization [6–8], feed forward control [5,9], sliding-mode control [10], and the super twisting algorithm with and without feedforward control [11,12] are such important and efficient techniques. Although an air mass flow sensor may be used to assess the oxygen excess ratio, it ruins the performance. This is because its time re-

*Correspondence: mhj_g@yahoo.com

sponse is about 1–2 s, which produces a long delay in the controller. The most common interest in [11–13] was using the airflow sensor specifically in a real-time application. However, sensor-based control has the following shortcomings:

- Slow response time (1–2 s),
- Short life time (6 months to 3 years),
- Less accuracy (1%–10%),
- Price (US$1000),
- Inevitable instrumental noise.

These restrictions are also applicable when the oxygen excess ratio is controlled through an inlet oxygen flow in the cathode ($W_{O2,in}$) measurement. Therefore, a sensorless approach is of interest in the current work. Talj et al. [14], in 2009, used a cascade structure for a PEMFC. Although their work had the advantages of a high-order sliding-mode (HOSM) controller, it again faced the following restrictions:

1. Sensor-based scheme has the above-mentioned drawbacks.
2. Instrumentation lag occurs in the overall system dynamic.
3. Since a nonsmooth input signal is generated to drive the motor, a ripple on the angular speed and then a ripple on the air flow are produced.

In the meantime, another cascade configuration was implemented by Matraji and Laghrouche [15]. A pressure and voltage transducer works with a fast time response, e.g., less than 1 ms. However, the air flow measurement needs a longer time lag of 1–2 s, which produces more lag on the system time response. This lag complicates the dynamic characteristics, especially when a sudden change in the load takes place. Since this effect is sensed after the prescribed lag, more force will act on the fuel cell and burn the membrane electrode assembly. Consequently, a finite time observer is required to estimate the oxygen excess ratio and some other unavailable states to improve the efficiency of the closed-loop system, and, in order to improve the dynamic response of a closed-loop feedback, a Kalman filter was used in [5,9]. In these works, primarily, the system is linearized about the operating point. Next, a Kalman observer is designed in the closed loop based on state feedback. However, the Kalman observer needs a linearized model with high accuracy that is still sensitive to uncertainties. This problem may be solved using Luenberger observers in state estimation [9,16]. In [17,18], a first-order sliding-mode observer was designed to estimate the states of a PEMFC system. The sliding-mode observer was based on a nonlinear model since it is robust to mismatched modeling errors and uncertainties. Unfortunately, the first-order sliding-mode approach has the following disadvantages [19]:

- For observation, filtering is needed, which corrupts the results.
- The need for filtering in the observation process destroys the finite time convergence property.

Furthermore, special attention must be paid to keeping the separation principle valid during the designation. In the current research, a finite time observer based on high-order sliding mode is proposed to estimate the oxygen excess ratio and some other relevant system states. A sixth-order model of the PEMFC system

is considered. The measured outputs are the compressor angular speed and the supply and return manifold pressures. The load current and input DC motor voltage are considered as the measured disturbance and control input, respectively. The observer control inputs are then constructed through a proper high-order sliding-mode algorithm. It will be shown that the state variables are estimated in finite time without the need for filtering or transformation in a regular form to ensure satisfaction of the separation principle.

The estimated oxygen excess ratio is then manipulated by 2 control approaches. Both control approaches propose to regulate the compressor supply voltage, v_{cm}, using sliding-mode control. The first approach uses 2 cascaded loops of second-order sliding mode (SOSM) based on a super twisting controller. This structure provides good tracking performance under large uncertainty of the motor parameters, fuel cell coefficients, and load current. The second approach uses a suboptimal controller in a single-loop structure. To verify the performance of the cascade structure, a comparison is made with respect to the suboptimal controller. Ultimately, the super twisting controller provides stability of the cascade structure. In order to address the above topics, this paper is organized as follows: A nonlinear model of the PEMFC is briefly introduced in Section 2. An observer is designed for a PEMFC system in Section 3, while the overall structure of the control scheme is designed in Section 4. In Section 5, simulation results are given to show the performance of the proposed scheme. Finally, a conclusion is given in Section 6.

2. Nonlinear dynamic of the PEMFC

A nonlinear model of a PEMFC stack in combination with some auxiliary equipment will be developed. Auxiliaries contain models of the compressor, air supply manifold, cathode humidifier, and fuel cell stack channels. Primarily, a ninth-order nonlinear model of the fuel cell system is considered [4,5,9]. This model describes the details of 75-kW fuel cell stack dynamics, fed by a 14-kW motor compressor.

2.1. Assumptions within the model

It is assumed that the fuel cell works under normal conditions. During normal conditions, the following assumptions are made. **A1:** The anode pressure is assumed to be constant. **A2:** The operating temperature and humidity of the air at the inlet of the fuel cell stack are constant. **A3:** Electric dynamics of the DC motor driving the compressor are also neglected. It should be noted that independent loops keep these assumptions valid.

The ninth-order model [4,5,9] is more complex and includes interactions (even if negligible) between 9 states, which makes the control harder. Therefore, order reduction from the ninth to sixth order usually takes place, e.g., as in [11] and [20]. Under the above assumptions, the model is reduced from the ninth order to the sixth while considering the states $x = [\omega_{cp}\ P_{sm}\ m_{sm}\ m_{O2}\ m_{N2}\ P_{rm}]^T$, whereas the concerned variables are defined in Table 1. These interconnections are theoretically investigated [4–8,11,13,21–23] such that the following compact form of the nonlinear state is derived. It is worth noting that the accuracy of the model is verified by comparing it with those in [11].

$$\dot{x}_1 = \tau_{cm} - \tau_{cp} = \frac{\eta_{cm}}{J_{cp}} \frac{k_t}{R_{cm}} (v_{cm} - k_v x_1) - \frac{\tau_{cp}}{J_{cp}} \tag{1}$$

$$\begin{aligned} \dot{x}_2 \quad = \quad & \tfrac{\gamma R_a}{V_{sm}} (-K_{sm,out} x_2 + K_{sm,out} P_{v,ca} + K_{sm,out} \tfrac{x_5}{M_{N2}} \tfrac{(R_{N2} T_{st})}{V_{ca}} \\ & + K_{sm,out} \tfrac{x_4}{M_{O2}} \tfrac{(R_{O2} T_{st})}{V_{ca}}) \tfrac{\gamma x_2}{x_3} + W_{cp} (T_{atm} + \tfrac{T_{atm}}{\eta_{cp}} (\tfrac{x_2}{P_{atm}})^{\frac{\gamma-1}{\gamma}} - 1)) \end{aligned} \tag{2}$$

Table 1. Key variables' descriptions.

State definition	Unit	Expresses
$x_1 = \omega_{cp}$	rad/s	Angular speed of the compressor
$x_2 = P_{sm}$	Pa	Supply manifold pressure
$x_3 = m_{sm}$	kg	Supply manifold air mass
$x_4 = m_{O2}$	kg	Oxygen mass at the cathode side
$x_5 = m_{N2}$	kg	Nitrogen mass at the cathode side
$x_6 = P_{rm}$	Pa	Return manifold pressure
$u = v_{cm}$	V	Compressor supply voltage; plant input
$d = I_{st}$	A	Stack current; measurable disturbance.

$$\dot{x}_3 = W_{cp} - K_{sm,out}x_2 + K_{sm,out}P_{v,ca} + K_{sm,out}\frac{x_5}{M_{N2}}\frac{(R_{N2}T_{st})}{V_{ca}} + K_{sm,out}\frac{x_4}{M_{O2}}\frac{(R_{O2}T_{st})}{V_{ca}} \tag{3}$$

$$\begin{aligned}\dot{x}_4 &= -\frac{x_4}{x_4+x_5+\frac{P_{v,ca}V_{ca}M_v}{R_vT_{st}}}K_{ca,out}(-x_6 + P_{v,ca} + \frac{x_5}{M_{N2}}\frac{(R_{N2}T_{st})}{V_{ca}} + \frac{x_4}{M_{O2}}\frac{(R_{O2}T_{st})}{V_{ca}}) \\ &\quad + y_{O2,in}K_{sm,out}(x_2 - \frac{x_4}{M_{O2}}\frac{(R_{O2}T_{st})}{V_{ca}} - P_{v,ca} - \frac{x_5}{M_{N2}}\frac{(R_{N2}T_{st})}{V_{ca}}) - n\frac{M_{O2}}{4\,F}I_{st}\end{aligned} \tag{4}$$

$$\begin{aligned}\dot{x}_5 &= (1 - X_{O_2,in})(1+\Omega_{atm})^{-1}K_{sm,out}(x_2 - \frac{x_4}{M_{O2}}\frac{R_{O2}T_{st}}{V_{ca}} - \frac{x_5}{M_{N2}}\frac{R_{N2}T_{st}}{V_{ca}} - P_{v,ca}) \\ &\quad - \frac{x_5}{x_4+x_5+\frac{P_{v,ca}V_{ca}M_v}{R_vT_{st}}}K_{ca,out}(-x_6 + \frac{x_4}{M_{O2}}\frac{R_{O2}T_{st}}{V_{ca}} + \frac{x_5}{M_{N2}}\frac{R_{N2}T_{st}}{V_{ca}} + P_{v,ca})\end{aligned} \tag{5}$$

$$\begin{aligned}\dot{x}_6 &= \frac{R_aT_{rm}}{V_{rm}}(K_{ca,out}(\frac{x_4}{M_{O2}}\frac{R_{O2}T_{st}}{V_{ca}} + \frac{x_5}{M_{N2}}\frac{R_{N2}T_{st}}{V_{ca}} + P_{v,ca} - x_6) \\ &\quad - (P_{a_6}x_6^5 + P_{a_5}x_6^4 + P_{a_4}x_6^3 + P_{a_3}x_6^2 + P_{a_2}x_6 + P_{a_1}))\end{aligned} \tag{6}$$

Here, τ_{cm} is the accelerating torque provided by the motor and τ_{cp} is the load torque, as in the following [22]:

$$\tau_{cp} = \frac{\pi}{30}(A_0 + A_1x_1 + A_{00} + A_{10}x_1 + A_{20}(x_1)^2 + A_{01}x_2 + A_{11}x_2x_1 + A_{02}(x_2)^2)), \tag{7}$$

where W_{cp} in Eq. (3) is the compressor air flow rate that depends on the compressor speed and the supply manifold pressure according to the following [22]:

$$W_{cp} = B_{00} + B_{10}x_2 + B_{20}(x_2)^2 + B_{01}x_1 + B_{11}x_2x_1 + B_{02}(x_1)^2, \tag{8}$$

where $M_a^{atm} = y_{O2,in}M_{O2} + (1 - y_{O2,in})M_{N2}$ is the molar mass of the air and $P_{v,ca} = \frac{m_{v,ca,\max}R_vT_{st}}{V_{ca}}$ stands for the vapor pressure in the cathode. The humidity ratio is defined by $\Omega_{atm} = \frac{M_v}{M_a^{atm}}\frac{\Phi_{atm}P_{sat,Tatm}}{P_{atm}}(1 - \frac{\Phi_{atm}P_{sat,Tatm}}{P_{atm}})^{-1}$. Reference values for the PEMFC model parameters are given in Tables 2, 3, and 4. Eqs. (1)–(6) can be written in the following general form, where $x \in \mathrm{R}^6$ is the system state and $f \in \mathrm{R}^6 \to \mathrm{R}^6$ is a continuous vector function representing the dynamics of the autonomous system.

$$\dot{x} = \begin{bmatrix} f_1(x_1, x_2) \\ f_2(x_1, x_2, x_3, x_4, x_5) \\ f_3(x_1, x_2, x_4, x_5) \\ f_4(x_2, x_4, x_5, x_6) \\ f_5(x_2, x_4, x_5, x_6) \\ f_6(x_4, x_5, x_6) \end{bmatrix} + \begin{bmatrix} \eta_{cm}\frac{k_t}{J_{cp}R_{cm}} \\ 0 \\ 0 \\ 0 \\ 0 \\ 0 \end{bmatrix} v_{cm} + \begin{bmatrix} 0 \\ 0 \\ 0 \\ -n\frac{M_{O2}}{4\,F} \\ 0 \\ 0 \end{bmatrix} I_{st} \tag{9}$$

Table 2. General parameters in the modeling of PEMFC.

Parameter	Symbol	SI units	Value
Atmospheric pressure	P_{atm}	Pa	101,325
Average ambient air relative humidity	Φ_{atm}	$--$	0. 5
Saturation pressure	$P_{sat,Tatm}$	Pa	3.1404×10^3
Atmospheric temperature	T_{atm}	K	298. 15
Air-specific heat ratio	γ	$--$	1. 4
Air density	C_p	$J\ kg^{-1}K^{-1}$	1004
Universal gas constant	R	$J\ mol^{-1}K^{-1}$	8. 31451
Air gas constant	R_a	$J\ mol^{-1}K^{-1}$	286. 9
Oxygen gas constant	R_{O2}	$J\ kg^{-1}K^{-1}$	259. 8
Nitrogen gas constant	R_{N2}	$J\ kg^{-1}K^{-1}$	296. 8
Vapor gas constant	R_v	$J\ kg^{-1}K^{-1}$	461. 5
Molar mass of air	M_a	kg/mol	28.97×10^{-3}
Molar mass of oxygen	M_{O2}	kg/mol	32×10^{-3}
Molar mass of nitrogen	M_{N2}	kg/mol	28×10^{-3}
Molar mass of vapor	M_v	kg/mol	18.02×10^{-3}
Faraday's constant	F	C/mol	96,487
Temperature of the fuel cell	T_{fc}	K	353

Table 3. Input parameters in the modeling of the PEMFC.

Parameter	Symbol	SI units	Value
Motor constant	K_t	Nm/A	0. 0153
Motor constant	R_{cm}	ohm	0. 82
Motor constant	K_v	$V/\ (rad/s)$	0. 0153
Compressor efficiency	η_{cp}	$--$	0. 8
Compressor motor mechanical efficiency	η_{cm}	$--$	0. 98
Number of cells in fuel cell stack	n	$--$	381
Fuel cell active area	A_{fc}	m^2	280×10^{-4}
Supply manifold volume	V_{sm}	m^3	0. 02
Single stack cathode volume	V_{ca}	m^3	0. 005
Return manifold volume	V_{rm}	m^3	0. 005
Supply manifold outlet orifice constant	$K_{sm,out}$	$kg\ s^{-1}\ Pa^{-1}$	0.3629×10^{-5}
Cathode outlet orifice constant	$K_{ca,out}$	$kg\ s^{-1}\ Pa^{-1}$	0.2177×10^{-5}
Compressor diameter	dc	m	0. 2286
Compressor and motor inertia	J_{cp}	$_{Nm}$	2×10^{-7}
Oxygen mole fraction at cathode inlet	$y_{O2,in}$	$--$	0. 21

3. HOSM observer for a PEMFC

3.1. Observer objective

The starvation phenomenon is an undesired issue that leads to the aging and degeneration of the fuel cell stack. Starvation takes place during transient changes in the stack current while reactants are consumed faster than

they are supplied, causing a severe decrease in the air flow in the cathode side. The best way to avoid oxygen starvation is fast regulation of the oxygen excess ratio through increasing the air mass flow in the cathode. Thus, the compressor must present a fast response against rapid variations in the load current. As a control objective, having accurate knowledge of the value of λ_{O2} is required. It depends on the ratio of 2 mass flows of inlet ($W_{O2,in}$) and reacting ($W_{O2,reacted}$) oxygen in the cathode side [10–12]. The oxygen excess ratio is defined via the following equation:

$$\lambda_{O2}=\frac{OxygenSupplied}{Oxygenreacted}=\frac{W_{O2,in}}{W_{O2,reacted}}. \tag{10}$$

One way to calculate λ_{O2} is by measuring inlet oxygen mass flow. Accordingly, the data must be acquired through sensors. However, practical mass flow measurement causes a time delay of about 1–2 s. Furthermore, available commercial mass flow meters are based on volumetric measurement, which is dependent on the liquid temperature. These direct methods have some restrictions in practical applications. The other way to evaluate λ_{O2} is to calculate the inlet and reacting oxygen mass flow through Eqs. (11) and (12). The reacting oxygen flow in the fuel cell stack is directly relevant to the measured stack current (I_{st}) [10]. Thus, it is calculated through Eq. (11).

$$W_{O2,reacted} = n\frac{M_{O2}}{4\,F}I_{st} \tag{11}$$

However, computation of the inlet oxygen flow is not straightforward, as it depends on states x_2, x_4, and x_5. Meanwhile, $W_{O2,in}$ is calculated via Eq. (12) as:

$$W_{O2,in} = X_{O_2,in}\frac{1}{(1+\Omega_{atm})}\,K_{sm,out}(x_2 - \frac{x_4}{M_{O2}}\frac{R_{O2}T_{st}}{V_{ca}} - \frac{x_5}{M_{N2}}\frac{R_{N2}T_{st}}{V_{ca}} - P_{v,ca}). \tag{12}$$

A substitution of Eqs. (11) and (12) into Eq. (10) immediately yields λ_{O2}. Governing constant parameters are defined in Tables 2–4. According to calculation of λ_{O2}, it is seen that λ_{O2} is related to the unmeasurable states x_4 and x_5. In this paper, due to the measurement problem of λ_{O2}, the unavailable states are estimated using an observer. Thus, a fast estimation of the air mass flow is required.

Table 4. Polynomial coefficients of equations.

B_{00}	$4.83\times10^{-5}kg/\sec$	P_{a_6}	0. 07804	A_{00}	0
B_{10}	$-5.42\times10^{-5}kg/\sec^2$	P_{a_5}	0. 02772	A_{10}	$0.0058Nm\sec$
B_{20}	$8.79\times10^{-6}kg/\sec^3$	P_{a_4}	0. 002122	A_{20}	$-0.0013Nm\sec^2$
B_{01}	$3.49\times10^{-7}kg\sec^2/bar$	P_{a_3}	-0.001524	A_{01}	$3.25\times10^{-6}Nm/bar$
B_{11}	$3.55\times10^{-13}kg/\sec$	P_{a_2}	-0.001967	A_{11}	$-2.80\times10^{-6}Nm\sec/bar$
B_{02}	$-4.11\times10^{-10}kg/\sec/bar$	P_{a_1}	0. 001248	A_{02}	$-1.37\times10^{-9}Nm\sec/bar^2$
		A_0	$4.1\times10^{-4}Nm$	A_1	$3.92\times10^{-6}Nm\sec$

3.2. Observability design requirements

The main aim of implementing an observer in our research is to estimate the oxygen and nitrogen masses at the cathode side, which form the oxygen excess ratio. Meanwhile, the HOSM observer estimates the oxygen excess ratio using pressure and angular speed measurements, as shown in Figure 1. Its observability is evaluated when

the compressor angular speed, supply, and return manifold pressures are regarded as measurable outputs and the stack current as a disturbance. Since these signals are usually available and easily measured, an output transformation for the system in Eq. (9) is applied as follows:

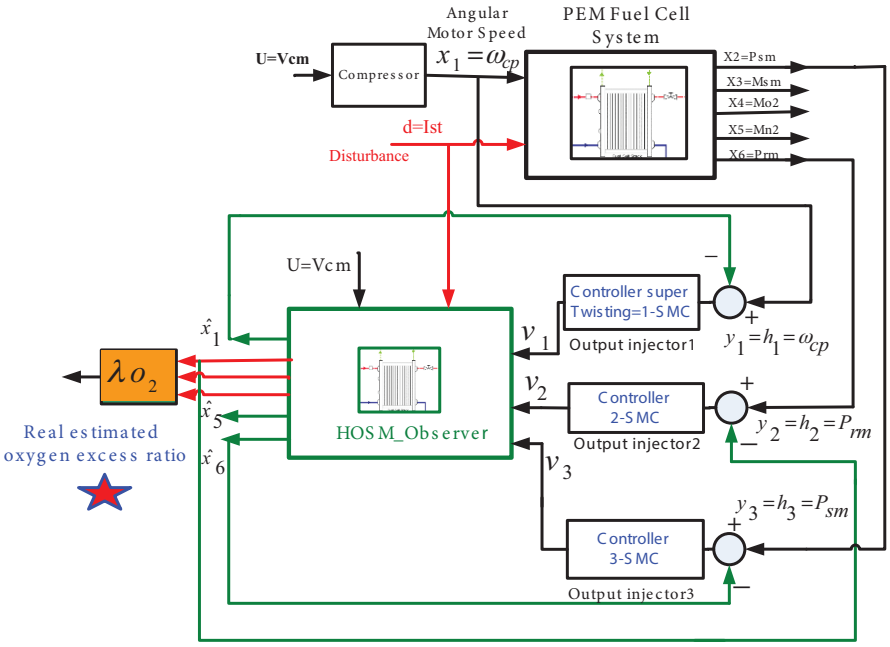

Figure 1. Plant with the observer configuration.

$$y=h(x)=\begin{bmatrix} h_1(x) \\ h_2(x) \\ h_3(x) \end{bmatrix}=Cx, C=[1\ \ 0\ \ 0\ \ 0\ \ 0\ \ 0\ \ ;\ \ 0\ \ 1\ \ 0\ \ 0\ \ 0\ \ 0\ \ ;\ \ 0\ \ 0\ \ 0\ \ 0\ \ 0\ \ 1]^T. \tag{13}$$

The observability needs the rank of the following matrix with a size of 12 $\times$ 6 to be of full rank.

$$\begin{aligned} &O_{sq}(\hat{x})=\left(\left[dh_1,\cdots,dL_f^{r_1-1}h_1,dh_2,\cdots,dL_f^{r_2-1}h_2,dh_3,\cdots,dL_f^{r_3-1}h_3\right]^T\right)_{12\times 6} \\ &\sum_{i=1}^{3} r_i=6, 0\le r_i\le 6, i=1,2,3 \end{aligned} \tag{14}$$

With reference to a generic scalar function, h_i with vector argument x is defined on an open set $\Omega\in \mathrm{R}^n$ and $h_i:\mathrm{R}^n\to\mathrm{R}$, where dh_i denotes: $dh_i=\frac{dh_i}{dx}=[\frac{dh_i}{dx_1},\frac{dh_i}{dx_2},...,\frac{dh_i}{dx_n}]$. L_fh_i is called the Lie derivative along $f(x)$ [24]. Due to the complexity of the defining system dynamics in Eqs. (1)–(6), the analytical evaluation of the rank of matrices in Eq. (14) appears to be an exhausting job. Accordingly, the rank of all possible submatrices is assessed. These are provided by any proper combination of rows in Eq. (14) in set M of the system state, including operation conditions, in the presence of possible admissible perturbations.

$$M=\left\{x\in \mathrm{R}^6:|x_i-x_i^*|<M_i, i=1,2,...,6\right\} \tag{15}$$

Here, $M_i(i=1,2,...,6)$ are known positive constants. Bound x_i can be found from prior knowledge of the system. For instance, the current can be increased up to $I_{st}\le 250[A]$, $5000\le x_1\le 12000[rad/\sec], 1.4\times 10^5\le$

$x_2 \leq 3.2 \times 10^5[Pa], 0.025 \leq x_3 \leq 0.05[kg], 1 \times 10^{-3} \leq x_4 \leq 3.5 \times 10^{-3}[kg], 0.006 \leq x_5 \leq 0.022[kg]$, and $1.2 \times 10^5 \leq x_6 \leq 2.6 \times 10^5[Pa]$.

Therefore, an alternative analytical approach is chosen to numerically assess the operation set M to find the minimum determinant of each square submatrix in Eq. (17). This means a solution for the following minimization problem:

$$J(x_{opt}) = \min_{x \in M} J(x), J(x) = \overset{2}{\det}(O_{sq}(\hat{x})) \neq 0, \tag{16}$$

where *det* stands for the determinant. To guarantee possible numerical, singularities are avoided, i.e. the precision is chosen to be large enough. If $J(x_{opt})$ is sufficiently far from 0, then the system of Eqs. (1)–(6) with the output in Eq. (13) are observable for any $x \in M$. As a result, the following reduced square observability matrix is found as nonsingular.

$$O_{sq}(\hat{x}) = \left[dh_1, dh_2, dL_f h_2, dh_3, dL_f h_3, dL_f^2 h_3\right]^T_{(6\times 6)} \tag{17}$$

This means that states can be estimated through a properly designed observer. The matrix in Eq. (17) is full rank in a sufficiently large set of working conditions. In the second stage, the minimum of Eq. (17) is assessed to verify the achievement, where the minimum of the index in Eq. (16) is listed in Table 5 for different randomly chosen starting conditions. An observer is inspired by Eq. (9) with scalar output $y \in \mathrm{R}, y = h(x)$. It is designed using the model including an extra additive output injection term. The acting observer dynamic is written as follows:

Table 5. Resuming for minimization.

Starting points	Minimized value $J(x) = \det^2(O_{sq}(\hat{x}))$
$x_{1(0)} = 5100; x_{2(0)} = 1.48 \times 10^5; x_{3(0)} = 0.03; x_{4(0)} = 1.2 \times 10^{-3}; x_{5(0)} = 0.008; x_{6(0)} = 1.28 \times 10^5$	$f_{\min} = 6.8472 \times 10^{46}$
$x_{1(0)} = 8100; x_{2(0)} = 1.97 \times 10^5; x_{3(0)} = 0.06; x_{4(0)} = 1.7 \times 10^{-3}; x_{5(0)} = 0.01; x_{6(0)} = 1.77 \times 10^5$	$f_{\min} = 1.5350 \times 10^{47}$
$x_{1(0)} = 11100; x_{2(0)} = 0.49 \times 10^5; x_{3(0)} = 0.1; x_{4(0)} = 2.7 \times 10^{-3}; x_{5(0)} = 0.09; x_{6(0)} = 2.46 \times 10^5$	$f_{\min} = 4.9088 \times 10^{39}$
$x_{1(0)} = 500; x_{2(0)} = 5.42 \times 10^5; x_{3(0)} = 0.03; x_{4(0)} = 1.2 \times 10^{-3}; x_{5(0)} = 0.8; x_{6(0)} = 4.24 \times 10^5$	$f_{\min} = 2.0368 \times 10^{52}$

$$\dot{\hat{x}} = f(\hat{x}) + gu + G(\hat{x}) \;\; v, \hat{y} = h(\hat{x}), \tag{18}$$

where vector $G(\hat{x})$ is the inverse of the last column of the observability matrix in Eq. (22). An output and state estimation error is defined by:

$$\bar{\varepsilon} = \hat{y} - y = h(\hat{x}) - h(x), e_x = \hat{x} - x, \tag{19}$$

$$\begin{aligned} \bar{\varepsilon}^{(j)} &= L^j_{f(\hat{x})} h(\hat{x}) - L^j_{f(x)} h(x), 1 \leq j \leq n-1 \\ \bar{\varepsilon}^{(n)} &= L^n_{f(\hat{x})} h(\hat{x}) - L^n_{f(x)} h(x) + v \end{aligned} \tag{20}$$

It is our aim to show that the error dynamic in Eq. (20) can be stabilized and converged in a finite time via an $n-$order sliding-mode algorithm. The required derivatives of the output error in the algorithm are

estimated through another high-order sliding-mode differentiator [25]. It is necessary to extend the approach to multiinput-multioutput (MIMO) systems [26], where the output injection gain matrix is designed such that the following relationship is met:

$$O_{sq}(\hat{x})G(\hat{x}) = N = \underbrace{\left[\begin{bmatrix} 0 & 0 & ... & 0 \\ \vdots & & & \\ 1 & 0 & ... & 0 \end{bmatrix}_{r_1\times p} \begin{bmatrix} 0 & 0 & ... & 0 \\ \vdots & & & \\ 0 & 1 & ... & 0 \end{bmatrix}_{r_2\times p} \cdots \begin{bmatrix} 0 & 0 & ... & 0 \\ \vdots & & & \\ 0 & 0 & ... & 1 \end{bmatrix}_{r_p\times p}\right]^T}_{N\ Matrix}, \tag{21}$$

$$G(\hat{x}) = (O_{sq}(\hat{x}))^{-1}N, \tag{22}$$

where $p$is the dimension of the output vector and $r_i(i = 1, 2, ..., p)$. This shows that the observation indices of the nonsingular matrix are of full rank.

Assumption 1 Matrix $O_{sq}(\hat{x})$ in Eq. (21) is nonsingular for every possible value of $\hat{x}$.

The proposed analytical approach in the previous subsection shows the observability indices as $r_1 = 1, r_2 = 2$, and $r_3 = 3$ for the PEMFC model in Eqs. (1)–(6) and (13). Therefore, the condition in Eq. (21) of the output injection gain matrix $G(\hat{x})$ has the following form:

$$O_{sq}(\hat{x})G(\hat{x}) = N = [1 \quad 0 \quad 0\ ;\ 0 \quad 0 \quad 0\ ;\ 0 \quad 1 \quad 0\ ;\ 0 \quad 0 \quad 0\ ;\ 0 \quad 0 \quad 0\ ;\ 0 \quad 0 \quad 1]^T. \tag{23}$$

Lemma 1 *Consider system Eq. (9) and assume $O_{sq}(\hat{x})$ to be nonsingular for every possible value of M. Next, the following implication holds:*

$$\bar{\varepsilon} = 0 \Leftrightarrow e_x = 0. \tag{24}$$

The state of the system in Eq. (9) can be reconstructed in finite time by applying the observers in Eqs. (18) and (22), provided that the correction term v_i is designed in such a way that error vector $\bar{\varepsilon}$ will be steered to 0 in finite time. □

Indeed, Lemma 1 proves the finite time convergence of the proposed observer. This means that the estimated states approach the real states in a limited time when the output injected terms v_i force the output error vector to tend to 0 in finite time. The proof of Lemma 1 is stated in Appendix 1.

3.3. Observer input design

An observer for the PEMFC can be designed according to the general form in Eqs. (18) and (22) as follows:

$$\begin{bmatrix} \dot{\hat{x}}_1 = \dot{\hat{\omega}}_{cp} \\ \dot{\hat{x}}_2 = \dot{\hat{P}}_{sm} \\ \dot{\hat{x}}_3 = \dot{\hat{M}}_{sm} \\ \dot{\hat{x}}_4 = \dot{\hat{M}}_{O2} \\ \dot{\hat{x}}_5 = \dot{\hat{M}}_{N2} \\ \dot{\hat{x}}_6 = \dot{\hat{P}}_{rm} \end{bmatrix} = \begin{bmatrix} f_1(\hat{x}_1, \hat{x}_2) \\ f_2(\hat{x}_1, \hat{x}_2, \hat{x}_3, \hat{x}_4, \hat{x}_5) \\ f_3(\hat{x}_1, \hat{x}_2, \hat{x}_4, \hat{x}_5) \\ f_4(\hat{x}_2, \hat{x}_4, \hat{x}_5, \hat{x}_6) \\ f_5(\hat{x}_2, \hat{x}_4, \hat{x}_5, \hat{x}_6) \\ f_6(\hat{x}_4, \hat{x}_5, \hat{x}_6) \end{bmatrix} + \begin{bmatrix} \eta_{cm}\frac{k_t}{J_{cp}R_{cm}} \\ 0 \\ 0 \\ 0 \\ 0 \\ 0 \end{bmatrix} u + \begin{bmatrix} 0 \\ 0 \\ 0 \\ -n\frac{M_{O2}}{4\,F} \\ 0 \\ 0 \end{bmatrix} \underbrace{I_{st} + O_{sq}^{-1}(\hat{x}) \begin{bmatrix} 1 & 0 & 0 \\ 0 & 0 & 0 \\ 0 & 1 & 0 \\ 0 & 0 & 0 \\ 0 & 0 & 0 \\ 0 & 0 & 1 \end{bmatrix}}_{G(\hat{x})} v. \tag{25}$$

The estimation error dynamics include the relative degree of the vector by $r=\{1,2,3\}$. The output vector $\hat{y}=[\hat{y}_1=\hat{\omega}_{cp},\hat{y}_2=\hat{P}_{rm},\hat{y}_3=\hat{P}_{sm}]$ forms output derivatives by:

$$e_1=\hat{y}_1-y_1=\hat{\omega}_{cp}-\omega_{cp},e_2=\hat{y}_2-y_2=\hat{P}_{rm}-P_{rm},e_3=\hat{y}_3-y_3=\hat{P}_{sm}-P_{sm}. \tag{26}$$

The vector of relative degree of $\{1,2,3\}$ is respectively relevant to the output vector $\{y_1,y_2,y_3\}$. It drives the observer control input v_i to be selected according to the relative degree. Each output injection term v_i can be designed by a high-order sliding-mode algorithm, such that the estimation error approaches 0 in a finite time. Therefore, output injection laws in the following are chosen according to each specific value of r_i (i.e. the relative degree):

- $r_1=1$ allows for using a super twisting algorithm [27] by

$$v_1=-\alpha_1\left|e_1\right|^{\frac{1}{2}}sign(e_1)-\lambda_1\int sign(e_1)dt. \tag{27}$$

- $r_2=2$ permits the use of a suboptimal algorithm [27] as

$$v_2=-\alpha_2U_2sign(e_2-\beta_2.e_{2,M}),\beta_2\in[0,1)\,. \tag{28}$$

- $r_3=3$ is suggested [28] to use a quasicontinuous algorithm. Since the output error $e_3=\hat{y}_3-y_3=\hat{P}_{sm}-P_{sm}$ contains a relative degree of 3, values are selected according to the third-order quasicontinuous sliding-mode algorithm as:

$$v_3=-\alpha_3\frac{\ddot{e}_3+2(|\dot{e}_3|+|e_3|^{\frac{2}{3}})^{\frac{1}{2}}(\dot{e}_3+|e_3|^{\frac{2}{3}}sign(e_3))}{|\ddot{e}_3|+2(|\dot{e}_3|+|e_3|^{\frac{2}{3}})^{\frac{1}{2}}}. \tag{29}$$

To implement the algorithm in Eq. (29), the values of $e_3,\dot{e}_3$, and $\ddot{e}_3$ must be configured. Since these terms are not actually available, a robust differentiation of e_3 is used to reconstruct the nonmeasurable variables. The following homogeneous differentiator of e_3 is proposed:

$$\begin{aligned}&\dot{z}_{3,0}=v_{3,0}\quad\text{where}\quad v_{3,0}=-\lambda_{3,0}\left|z_{3,0}-e_3\right|^{\frac{2}{3}}sign(z_{3,0}-e_3)+z_{3,1}\\&\dot{z}_{3,1}=v_{3,1}\quad\text{and}\quad v_{3,1}=-\lambda_{3,1}\left|z_{3,1}-v_{3,0}\right|^{\frac{1}{2}}sign(z_{3,1}-v_{3,0})+z_{3,2}\end{aligned} \tag{30}$$

Parameters of the algorithm in Eq. (29) and differentiator in Eq. (30) are tuned according to the bounds of the observer dynamics. Proper positive constant coefficients $\lambda_{3,i}$ are chosen large enough in the given order [25] under the assumption that a constant L exists such that $\left|e^{(n)}\right|<L$. After a finite-time transient process, the following equalities are satisfied, of course in the absence of measurement noise: $\left|Z_3-e_3^{(i)}\right|=0$ and $i=0,1,...,n$. It was demonstrated by Levant in [25] that nonidealities, such as measurement noise and finite frequency commutation, cause a bounded error in the estimated derivatives. As a result, a bounded loss of accuracy occurs, which causes the algorithm to use 'noisy' derivative estimates [25,28].

4. Structure of the overall control scheme

Starvation is one of the main causes of aging of the fuel cell. Oxygen starvation causes performance degradation in the fuel cell and a cell voltage drop occurs. To avoid the oxygen starvation phenomenon, the oxygen excess ratio should be adjusted quickly. Thus, regulating the compressor voltage v_{cm} causes a rapid increase in the mass flow into the cathode and the prevention of oxygen starvation. This regulation prolongs the fuel cell life and optimizes the performance. When a step change in current I_{st} occurs, compressor voltage v_{cm} has to be properly adjusted to regulate the oxygen excess ratio. The proposed overall control scheme consists of the following 2 nested loops using SOSM-based control:

1. An inner loop generates the reference compressor voltage by controlling the angular speed.

2. An outer loop provides a reference angular motor speed by controlling the oxygen excess ratio.

An effective solution to stabilize the control loop is a cascade structure via using a super twisting controller. In this configuration, 2 nested loops are provided, as shown in Figure 2. The inner loop forms a proper control signal to accordingly change the angular speed of the motor. The outer loop is designed to control the excess ratio when the constructed λ_{O2} is compared with the reference λ^*_{O2} to form the error signal. The error is then processed by a super twisting controller to generate an angular speed reference applied to the inner loop.

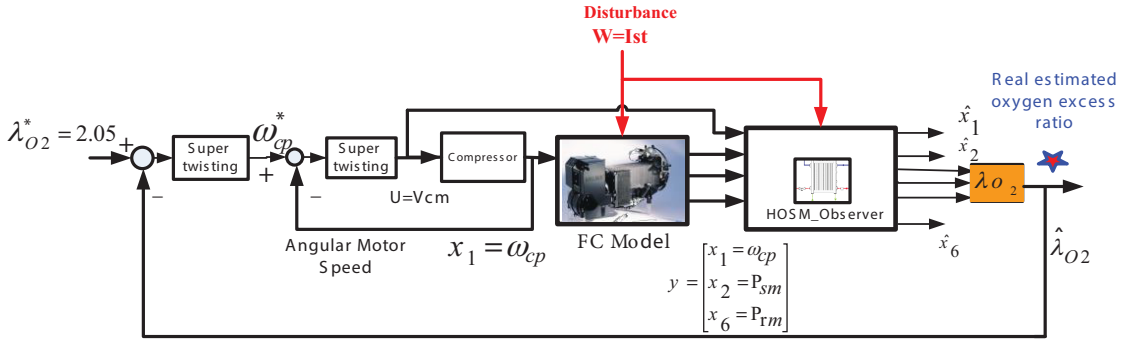

Figure 2. Block diagram of the proposed cascade structure using a super twisting controller.

4.1. Cascade structure

The super twisting controller consists of a control output u with 2 terms, without the need for information on $\dot{S}$. The first term is a discontinuous time-derivative term, while the second is a continuous function of a sliding variable. Thus, the $u$control law is defined by the following expression:

$$u = -\lambda |S|^{\frac{1}{2}} sign(S) - W \int_0^t sign(S(\tau))d\tau, \tag{31}$$

where W and λ are design parameters. The first-time derivative of the sliding variable is expressed by $\dot{S} = \phi(t,x) + \gamma(t,x)u$. Terms $\gamma(t,x)$ and $\phi(t,x)$ are functions in time and the states. For PEMFC system applications, they are bounded smooth functions as $0 < \Gamma_m \leq \gamma(t,x) \leq \Gamma_M$ and $|\phi(t,x)| \leq \Phi$, where Φ, Γ_M, and $\Gamma_m$are appropriate bounds. Sufficient conditions for finite time convergence of the sliding manifold Scan be seen in [29]:

$$W > \frac{\Phi}{\Gamma_m}, \lambda^2 \geq \frac{4\Phi}{\Gamma_m^2}\frac{\Gamma_M(W+\Phi)}{\Gamma_m(W-\Phi)}. \tag{32}$$

The required controller parameters are properly designed to meet the conditions in Eq. (32). Therefore, convergence of the super twisting controller in finite time is guaranteed. This controller provides proper performance in systems with relative degrees of 1 and shows good robustness against disturbances and uncertainties [27]. Furthermore, this is found effective for chattering attenuation purposes.

4.1.1. Inner control loop

The aim of this loop is to provide the oxygen ratio through the compressor. The inner loop provides the measured angular speed (ω_{cp}) in a quicker time through a separate controller using the reference angular speed (ω^*_{cp}). This loop produces an actual control input v_{cm} to ensure quick convergence of the measured angular speed to the reference angular speed. This control objective will be achieved under the variable structure system (VSS) theory framework, i.e. sliding-mode control. To implement this controller, first a sliding surface must be defined as a discrepancy between the real motor speed and that of the command. This can be found by:

$$S_2 = \omega_{cp} - \omega^*_{cp}. \tag{33}$$

Once the differentiation of the sliding variable $S_2 = \omega_{cp} - \omega^*_{cp}$ of the inner loop is complete, the control input v_{cm} will appear in the first derivative, as seen in Eq. (A7) of Appendix 2. This equation verifies that the relative degree between the angular speed and the compressor voltage is 1. A detailed description of the first-order derivative $\dot{S}_2$ along with coefficients $\gamma_2(t,x)$ and $\varphi_2(t,x)$ is given in Appendix 2.

$$0 < \Gamma_{2,m} \leq \gamma_2(t,x) \leq \Gamma_{2,M}, |\phi_2(t,x)| \leq \Phi_2 \tag{34}$$

To form the control in Eq. (34), the parameters of the controller have to be determined using sufficient conditions in Eq. (32). Therefore, it is necessary to find the bound of the first derivative of the sliding surface, such that the following bounded conditions on the sliding dynamics are satisfied. The closed-loop error dynamics are then bounded by:

$$\dot{S}_2 \in [-\Phi_2, \Phi_2] + [-\Gamma_{2,m}, \Gamma_{2,M}]\, v_{cm}, \tag{35}$$

considering the positive constants $\Gamma_{2,m}, \Gamma_{2,M}$, and Φ_2. Substitution of the states in $\dot{S}_2$ (Appendix 2) evaluates the bounds of γ_2 and Φ_2 in $0 < \Gamma_{2,m} \leq \gamma_2(t,x) \leq \Gamma_{2,M}$ and $|\phi_2(t,x)| \leq \Phi_2$. On the other hand, a bound for the sliding surface is arbitrarily chosen, which is seen here as $S_{2,0} = 1 \times 10^{-3}$. This yields $5717.69 \leq \gamma_2 \leq 6675.88$ and $\Phi_2 = 0.6455$. To achieve finite time convergence of the angular speed, the following theorem must be satisfied.

Theorem 1 *The error of the angular speed tracking in the inner loop converges to $S_2 = 0$ in finite time. An upper bound of the convergence time is assessed by the following:*

$$T_{0,inner} = \frac{2\, V^{\frac{1}{2}}(\zeta_{inner}(0))}{\alpha} = \frac{2\sqrt{\zeta^T_{inner}(0)\ \ Q\ \ \zeta_{inner}(0)}}{\alpha}, \alpha = \frac{\lambda_{\min}\{Q\}\ \ \lambda^{\frac{1}{2}}_{\min}\{P\}}{2\lambda_{\max}\{P\}}, \tag{36}$$

where $\zeta_{inner}(0)$ is an initial condition of ζ_{inner}. □

Proof of Theorem 1:
Consider the following super twisting controller:

$$\dot{Z}_1 = -K_1 |Z_1|^{\frac{1}{2}} sign(Z_1) + Z_2, \dot{Z}_2 = -K_2 sign(Z_1), \tag{37}$$

where $Z_1 \in \mathrm{R}$ and $Z_2 \in \mathrm{R}$ concerning the equilibrium point at $(Z_1, Z_2) = (0,0)$. A detailed stability proof of the super twisting controller can be found in [30–32]. Now consider the following family of quadratic Lyapunov functions [30]:

$$V = \zeta^T P \zeta, \tag{38}$$

such that $\zeta = [|Z_1|^{\frac{1}{2}} sign(Z_1), Z_2]^T$, where P is a positive definite matrix [33]. Function $V(t)$ is continuous and differentiable, except when $Z_1 = 0$. In fact, for $Z_1 \neq 0$, its derivative, $\dot{V}(\zeta, t)$, exists and is negative-definite. It can be seen that although the state trajectory of Eq. (38) attaches to the surface S_2, it cannot stay on it. Before reaching the equilibrium point $(Z_1, Z_2) = (0,0)$, Eq. (37) coincides with the line $Z_1 = 0$ for $Z_2 \neq 0$. This means that the derivative of the Lyapunov function exists everywhere until the state trajectory reaches the equilibrium point. In accordance with [30,31,33], $V(t)$ is a strong Lyapunov function of the form of Eq. (38) for Eq. (37). Although this Lyapunov function is positive-definite, it is radially unbounded.

$$\lambda_{\min}(P) \|\zeta\|_2^2 \leq V \leq \lambda_{\max}(P) \|\zeta\|_2^2, \tag{39}$$

when $\|\zeta\|_2^2 = |Z_1| + Z_2^2$ stands for an Euclidian norm of ζ. The construction of proper positive definite matrices $P = P^T$ solves the algebraic Lyapunov equation (ALE) of [30,31,33]:

$$A^T P + PA = -Q, \tag{40}$$

where $A = \begin{bmatrix} -K_1 & 1 \\ -K_2 & 0 \end{bmatrix}$, $K_1 > 0$ and $K_2 > 0$, are positive gains. This means that matrix A is Hurwitz, where $Q = Q^T > 0$ is an arbitrary chosen symmetric and positive definite matrix. Using the vector $\zeta = [|Z_1|^{\frac{1}{2}} sign(Z_1), Z_2]^T$, since $\dot{\zeta} = \begin{bmatrix} -K_1 & 1 \\ -K_2 & 0 \end{bmatrix} \zeta \Big/ (2|Z_1|^{\frac{1}{2}}) = A\zeta \Big/ (2|Z_1|^{\frac{1}{2}})$, the derivative of the Lyapunov function is obtained as:

$$\dot{V}(\zeta) = \dot{\zeta}^T P \zeta + \zeta^T P \dot{\zeta} = \frac{1}{2|Z_1|^{\frac{1}{2}}} \zeta^T (A^T P + PA) \zeta = -\frac{1}{2|Z_1|^{\frac{1}{2}}} \zeta^T Q \zeta. \tag{41}$$

According to Eq. (39) and the Euclidian norm of ζ, it is seen that $\|\zeta\|_2 \leq V^{\frac{1}{2}}(\zeta) \Big/ (\lambda_{\min}^{\frac{1}{2}}\{P\})$. Therefore, $\dot{V}(\zeta, t)$ is deduced by:

$$\dot{V}(\zeta) = -\frac{1}{2|Z_1|^{\frac{1}{2}}} \zeta^T Q \zeta \leq -\frac{\lambda_{\min}\{Q\}}{2|Z_1|^{\frac{1}{2}}} \|\zeta\|_2^2 \leq -\frac{\lambda_{\min}\{Q\} \lambda_{\min}^{\frac{1}{2}}\{P\}}{2\lambda_{\max}^{\frac{1}{2}}\{P\}} V^{\frac{1}{2}}(\zeta), \tag{42}$$

where $\alpha = \lambda_{\min}\{Q\} \lambda_{\min}^{\frac{1}{2}}\{P\} \Big/ (2\lambda_{\max}^{\frac{1}{2}}\{P\})$ and $\dot{V} \leq -\alpha V^{\frac{1}{2}}(\zeta)$. Therefore, the finite time convergence of vector (Z_1, Z_2) to 0 is guaranteed and bounded by $T_0 = 2V^{\frac{1}{2}}(\zeta(0)) \Big/ \alpha$, assuming that $\zeta(0)$ is the initial value

of ζ. It was suggested in [32] that the identity matrix selection as $Q = I$ is a proper choice to achieve a minimum time for a class of Lyapunov functions. Choosing $\mathrm{K}_1 = 0.45$ and $\mathrm{K}_2 = 0.8$ results in $P = \left[2\frac{1}{2}; -\frac{1}{2}2.781\right]^T$ by $P = P^T > 0$ as a solution of the ALE. The initial conditions of $Z_1(0) = 0.69$ and $Z_2(0) = 0.14$, an estimation of the upper bound of the convergence time $T_{0,inner} = 2V^{\frac{1}{2}}(\zeta_{inner}(0))\Big/\alpha$, is found as $T_{0,inner} = 3.46$.

4.1.2. Outer control loop

The main task of the outer loop is to derive the oxygen excess ratio λ_{O2} to its desired oxygen excess ratio reference value λ^*_{O2} through the generation and adjustment of the compressor angular speed. Indeed, a super twisting controller must force the sliding variables $S_1 = \lambda_{O2} - \lambda^*_{O2}$ to 0 in finite time. Primarily, a relative degree is equal to 1 when the first derivative of variable S_1 is taken (Eq. (A8) of Appendix 2). By replacing $\dot{x}_2$ from Eq. (2) into Eq. (A8), a direct relationship between $\dot{\lambda}_{O2}$ and ω_{cp} will be achieved. The result shows the relative degree of 1 between the oxygen excess ratio and the angular motor speed. Similarly, there is a relative degree of 2 between the oxygen excess ratio and the compressor voltage. The closed-loop error dynamics in the outer loop are then bounded by:

$$\dot{S}_1 \in [-\Phi_1, \Phi_1] + [-\Gamma_{1,m}, \Gamma_{1,M}]\,\omega_{cp}. \tag{43}$$

The system bound, similar to $S_{2,0}$, is arbitrarily chosen as $S_{1,0} = 1 \times 10^{-3}$. This again obtains the following bound:

$$\begin{array}{l} 0 < \Gamma_{1,m} \le \gamma_1(t,x) \le \Gamma_{1,\,M}, |\phi_1(t,x)| \le \Phi_1 \\ 3.492 \times 10^{-7} \le \gamma_1 \le 6.984 \times 10^{-\,5}\,,\, \Phi_1 = 2.345 \times 10^{-\,7} \end{array}. \tag{44}$$

Detailed descriptions of the first-order derivatives $\dot{S}_1$ and $\dot{S}_2$, along with the coefficients $\gamma_1(t,x), \phi_1(t,x)$, and $\gamma_2(t,x), \phi_2(t,x)$, are given in Appendix 2. In order to obtain a finite-time convergence of reaching the estimated oxygen excess ratio to the sliding surface, the following theorem must be valid.

Theorem 2 *Similar to the method in Theorem 1, the oxygen excess ratio in the outer loop converges to equilibrium λ^*_{O2} in a finite time of $T_{0,outer}$, which is expressed in the following:*

$$T_{0,outer} = \frac{2\sqrt{\zeta^T_{outer}(0)\;\; Q \;\; \zeta_{outer}(0)}}{\alpha}, \alpha = \frac{\lambda_{\min}\{Q\}\;\; \lambda^{\frac{1}{2}}_{\min}\{P\}}{2\lambda_{\max}\{P\}}. \tag{45}$$

Proof The determination of the convergence time of the outer loop can be proven in the same way as in Theorem 1. □

Coefficients of super twisting in the inner and outer loops of the cascade structure are found by a trade-off between the dynamic performance and chattering as $\lambda_1 = 2, W_1 = 2$, and $\lambda_2 = 4, W_2 = 4$.

Proposition 1 *The sliding mode controller in Eq. (31) guarantees that the system in Eq. (9) tracks and converges to the reference command in finite time if the observer in Eq. (25) constructs unavailable states in finite time. On the other hand, when the observer dynamics are fast enough to provide an accurate evaluation of the modes, the controller stabilizes the whole closed-loop system.*

Satisfaction 1 *According to Lemma 1 and the finite time convergence of observer, it is not necessary to prove the separation principle [25,34,35]. Considering the separation principle using HOSM observers in a VSS, a general statement is that if the observation is achieved in a finite time and the system is bounded-input bounded-output stable, it is possible to design an observer and controller separately. This means that after a finite time, the estimation error vanishes and, therefore, the state feedback can be implemented using the state estimates [34,35]. Next, it is sufficient to prove a finite time convergence of the observer (Lemma 1) and the stability of the system in a closed loop (Section 4.1) with super twisting control separately.*

4.2. Suboptimal controller

To investigate the validity and performance of the proposed cascade structure, a suboptimal controller is used as an alternative technique. The control objective is $S(x,t) = \lambda_{O2} - \lambda_{O2}^*$, which again needs to become 0. As previously stated, the control signal $u = v_{cm}$ appears in the second-order derivative of the sliding variable $S(x,t) = \lambda_{O2} - \lambda_{O2}^*$; therefore, the relative degree is again found as 2. A block diagram of the system under suboptimal control is shown in Figure 3. Moreover, during a real-time application, the suboptimal controller only requires knowledge of the sign of the sliding variable. The main advantage of this approach relies on its robustness against some parametric uncertainties and external disturbances. This controller is used for plants with a relative degree of 2, as in the following [27]:

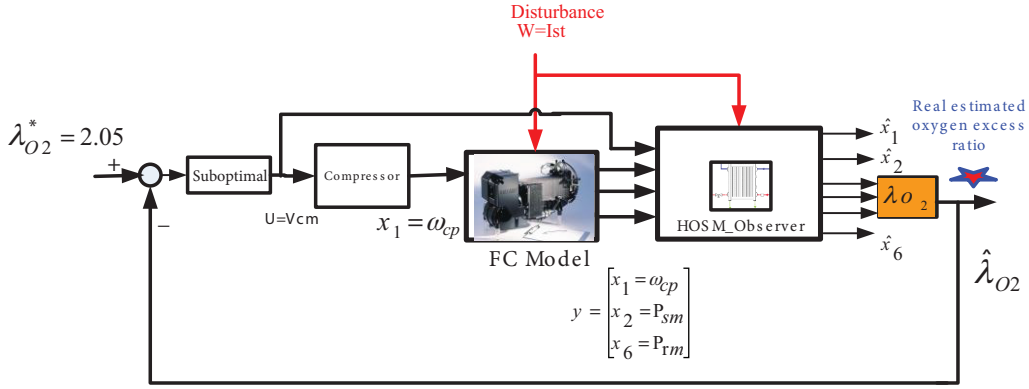

Figure 3. Block diagram of the controlled system with a suboptimal controller.

$$u(t) = -\alpha(t) U \; sign(S - \beta S_M)$$
$$\beta \in [0,1), \alpha(t) = \begin{cases} 1 & \text{if} \quad (S - \beta S_M) S_M \geq 0 \\ \alpha^* & \text{if} \quad (S - \beta S_M) S_M < 0 \end{cases}, \tag{46}$$

where α^*, β, and U are controller parameters. These must be tuned according to the following inequalities:

$$U > \frac{\Phi}{\Gamma_m}, \alpha^* \in [1, +\infty) \cap \left[\frac{\Phi + (1-\beta)\Gamma_M U}{\beta \Gamma_m U}, +\infty \right). \tag{47}$$

Finally, the parameters of the suboptimal controller in Eq. (47) are selected as $\beta = 0.9, U = 1$, and $\alpha^* = 1$.

5. Simulation results

In order to verify the performance of the proposed configuration, including 2 individual controllers (used in the cascade and also the suboptimal) in combination with the proposed finite-time observer, several simulations are carried out. Since the temperature and humidity are assumed to be constant, a separate controller is designed to keep them unchanged to validate those assumptions. Meanwhile, the bounds of the estimation error dynamics are overestimated due to consideration of the worst-case design during the state variations within set M in Eq. (16). Meanwhile, the parameters of the output injection law in Eqs. (27)–(30) are manually tuned. All of the simulations are performed in Table 6 with the set configuration and parameters of the output injection law. The load current is stepped up from 100 A to 150 A at t = 20 s, after 35 s. It is again stepped down to 120 A, and, finally, at time t = 80 s, the current is stepped up from 120 A to 190 A (Figure 4).

Table 6. Output injectors and parameter settings according to the relative degrees.

Relative degree	Type of controller	Parameter tunings
$r_1 = 1$	Super twisting algorithm	$\lambda_1 = 3, \alpha_1 = 3$
$r_2 = 2$	Suboptimal algorithm	$\beta_2 = 0.5, U_2 = 0.1, \alpha_2 = 1$
$r_3 = 3$	Quasi-continuous algorithm	$n = 2, \lambda_{3,0} = 15.9, \lambda_{3,1} = 33.5,$ $\lambda_{3,2} = 550, \alpha_3 = 1500$

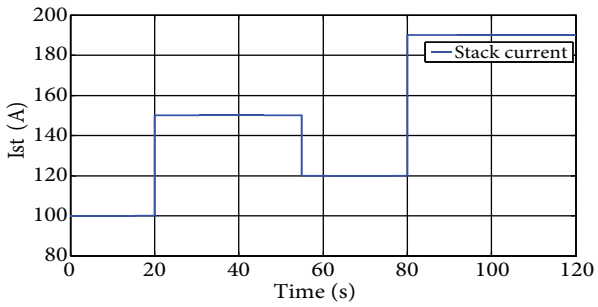

Figure 4. Load current variation profile.

5.1. Observer analysis for estimation of the oxygen excess ratio

In the observer analysis, the voltage driving the DC motor of the compressor is maintained constant at 150 V. The goal of the observer design is to estimate an unmeasurable state of the PEMFC, i.e. the oxygen excess ratio, which is expressed from Eqs. (10) through (12). Actual and estimated values of the oxygen excess ratio are illustrated in Figure 5. It is seen that the important variable to improve the efficiency of the PEMFC is precisely estimated. To verify the tracking ability of the observer, the oxygen excess ratio is estimated using the HOSM observer, which is depicted in Figure 5. Since the error band is narrow, the outcome of the estimation is found satisfactory. Figure 5 also shows that the estimator follows the oxygen excess ratio with an acceptable lag. The observer converges to the correct amount of the oxygen excess ratio in a finite time, i.e. after approximately 3 s. It is seen that the proposed observer is capable to estimate some important states of the PEMFC and the oxygen excess ratio in finite time. Furthermore, a sliding-mode technique is developed in the observer design. This also produces an output injection with a high switching frequency and zero mean value.

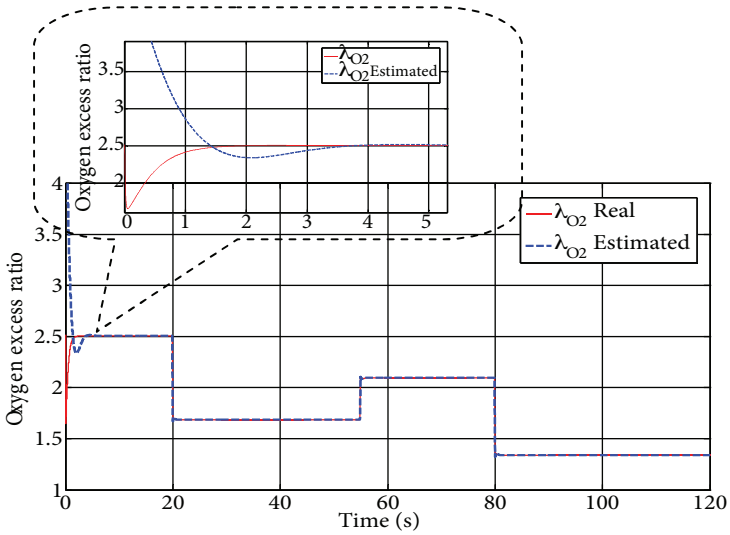

Figure 5. Estimation of the oxygen excess ratio signal.

5.2. Output feedback control system

An optimum value of $\lambda^*_{O2} = 2.05$ [4,5] is assumed as a reference. It can be assured that the system works at its maximum net power for each load variation. To verify the performance of the proposed control structure, some simulations are carried out. The following results are achieved from different implementations of the closed-loop system.

In TEST 1, since the relative degree equals 2, a suboptimal controller is implemented as in Figure 6a.

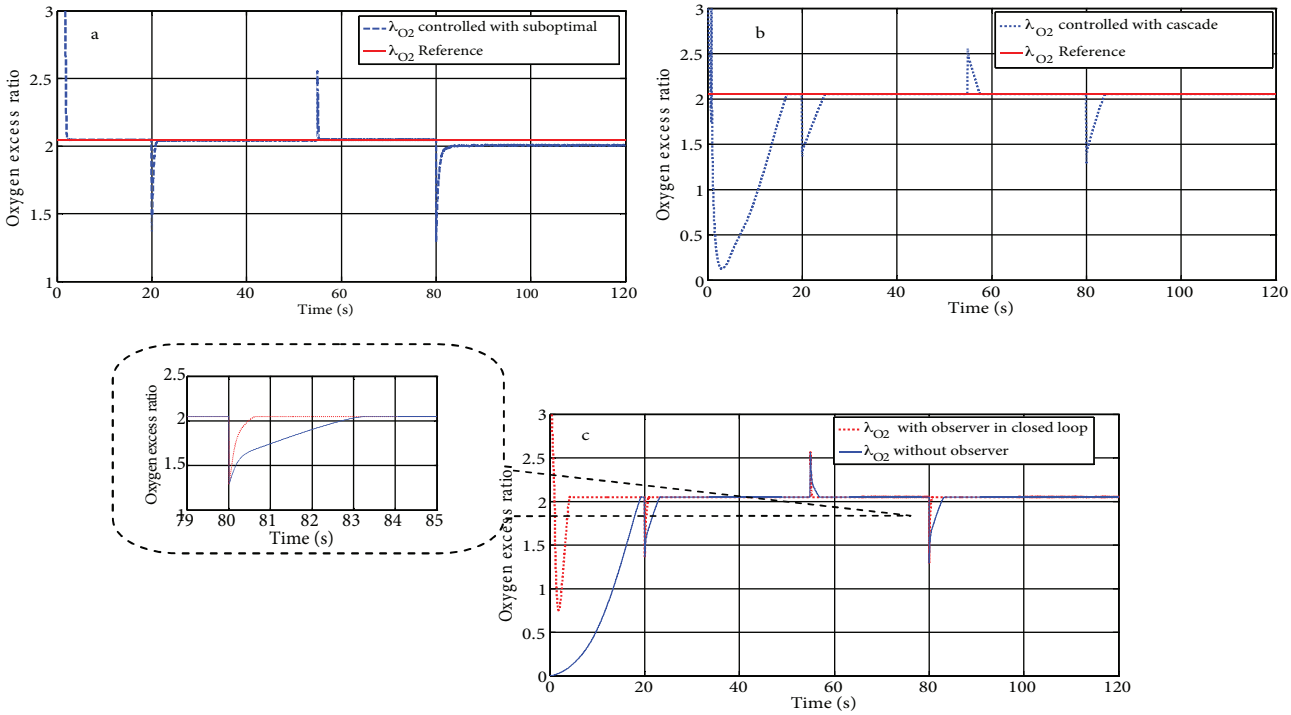

Figure 6. a) Oxygen excess ratio control via the suboptimal controller, b) cascade structure, and c) oxygen excess ratio control with an observer and without an observer.

In TEST 2, a cascade structure with a super twisting controller is implemented. The dynamic behavior of the oxygen excess ratio under different load conditions is also depicted in Figure 6b. It can be observed that this variable follows the reference well enough with satisfactory tracking performance.

According to the graphs, it is found that the suboptimal controller produces a faster time response with respect to the cascade structure. However, the error band in the cascade structure using the super twisting controller is found as smaller and narrower with respect to the suboptimal controller. From the simulation results, it can be stated that the suboptimal controller presents good dynamic behavior. This controller reduces the rise time and settling time of tuning the oxygen excess ratio during the transient step changes of the current with respect to the cascade structure (Table 7).

Table 7. Time domain performance specifications.

Controller type	Rise time (ms)	Settling time (ms) (3%)	Output deviations
Cascade	3950	5130	$\pm 2.5 \times 10^{-4}$
Suboptimal	61	1220	$\pm 3 \times 10^{-3}$

In the meantime, the performance of the proposed observer can be compared with that of the actual states in [11]. The result in Figure 6c shows that without using the observer, the system tracks the reference value of λ_{O2} in about 3 s, whereas in the closed-loop implementation, using the observer significantly reduces the tracking time to 0.4 s.

However, this produces a control input with a high switching voltage, which is undesired for the motor of the compressor (Figure 7a). Furthermore, a large variation in the control input is undesired in the control applications. In contrast to the suboptimal controller, the cascade implementation of the super twisting controller provides a smooth voltage input in Figure 7b. Sliding surface variations $S(t)$ during the control procedure are also illustrated in Figures 8a and 8b when suboptimal control and the cascade structure are of interest, respectively. For a small error signal, surface $S(t)$ reaches a value close to 0, which means that the oxygen excess ratio follows the reference command. Meanwhile, system trajectories are plotted in the phase plane in terms of $\dot{S}(t)$ and $S(t)$ for the suboptimal control system. Those $\dot{S}(t)$ and $S(t)$ values for the super twisting controller in the cascade structure are also plotted in Figures 9a and 9b, respectively. The phase portrait of the system $\dot{S}(t) - S(t)$ presents a nonuniform characteristic of the super twisting controller. Those results confirm that both $\dot{S}(t)$ and $S(t)$ converge to 0 via the super twisting and suboptimal controller.

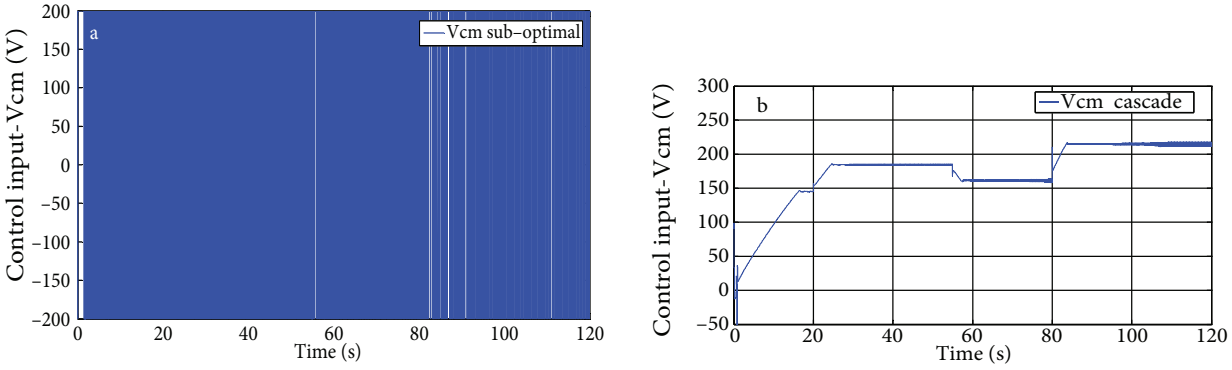

Figure 7. Control effort of the a) suboptimal control and b) cascade structure.

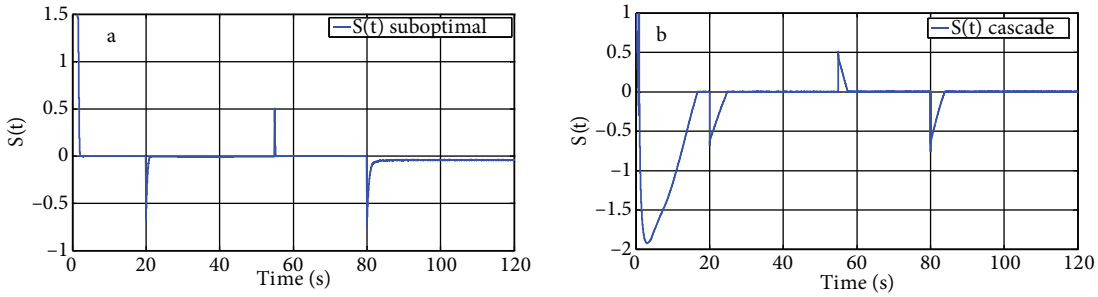

Figure 8. Sliding surface of the a) suboptimal controller and b) cascade structure.

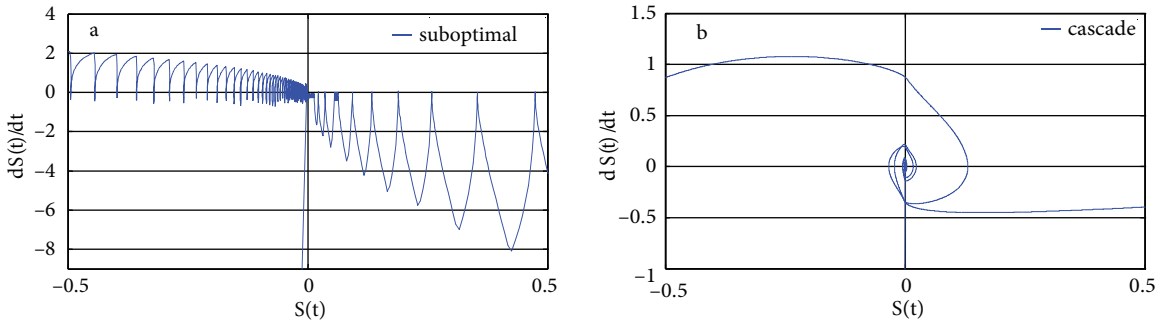

Figure 9. Phase portrait $\dot{S}(t)$ and $S(t)$ of the a) suboptimal controller and b) cascade structure.

To verify the system tracking performance, the closed-loop system undergoes a further test in an optimal oxygen excess ratio range of 2.05–2.5. Accordingly, a square wave with an amplitude of between 2.05 and 2.5 is applied to the system. Results are shown in Figures 10a and 10b for the suboptimal control system and another controller in the cascade structure, respectively. The results confirm that the controller in the cascade structure provides better tracking performance when it presents less variation in the steady state with respect to the suboptimal controller. Nonetheless, the suboptimal controller converges faster than the cascade structure.

6. Conclusion

In this paper, a proper MIMO nonlinear observer, based on high-order sliding mode, was applied in a PEMFC. The observer was shown to be convergent in finite time without the need for transformation. It is based on an analysis of the structural properties of the observability matrix of the system. The estimated oxygen excess ratio was controlled in a closed-loop system using 2 distinct approaches of cascade and suboptimal structures. These approaches showed improvement in the transient response.

In the cascade structure, it could be observed that the oxygen excess ratio satisfactorily tracked the reference. In addition, the error band in the cascade scheme with super twisting was narrower. In comparison, the proposed suboptimal application provided faster convergence to the sliding surface. Use of the proposed control schemes gains the following benefits:

1. It enhances the dynamic characteristics; the use of an observer-based feedback controller reduces the rise time and settling time for the oxygen excess ratio during the transient load variation.

2. During the estimation of the state, instrumentation noise has less affect in the system with respect to the case when states are measured.

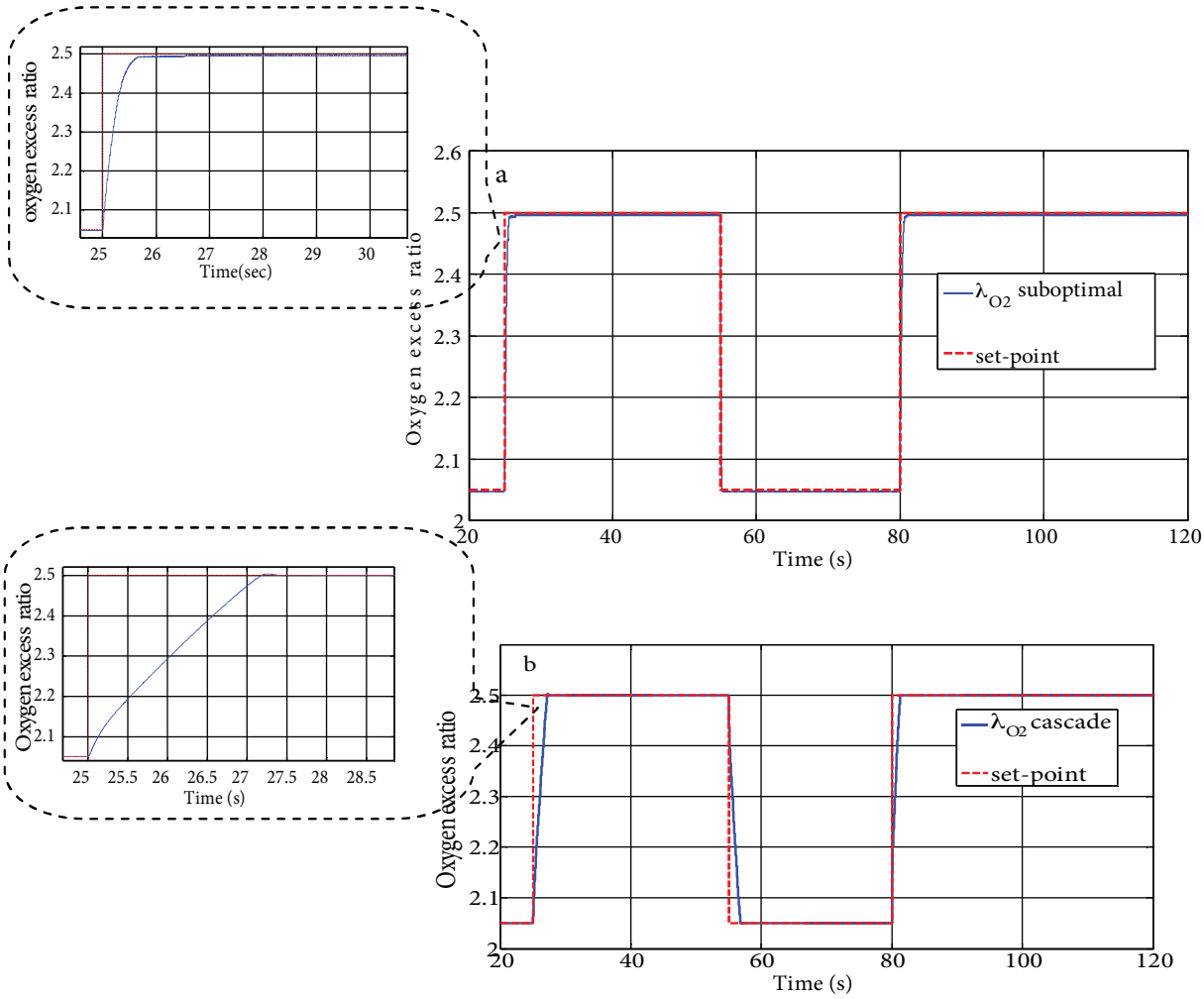

Figure 10. Tracking results of the suboptimal and cascade structures.

Due to the close relation between the current study and practical implementation, a hardware control is promising but complex.

Appendix 1. Proof of Lemma 1.

Define the output and state observation errors:

$$\bar{\varepsilon} = \hat{y} - y = [\bar{e}_1 \bar{e}_2 \dot{\bar{e}}_2 \bar{e}_3 \dot{\bar{e}}_3 \ddot{\bar{e}}_3]^T \ , \quad e_x = \hat{x} - x = [e_{x_1} e_{x_2} e_{x_3} e_{x_4} e_{x_5} e_{x_6}]^T . \tag{A1}$$

The output error $\bar{\varepsilon} = \hat{y} - y$ possesses the same relative degree $sr_1 = 1$, $r_2 = 2$, and $r_3 = 3$ with respect to v_1, v_2, and v_3.

$$e_x = \hat{x} - x = [e_{x_1} e_{x_2} e_{x_3} e_{x_4} e_{x_5} e_{x_6}]^T \Rightarrow \dot{e}_x = \dot{\hat{x}} - \dot{x} = f(\hat{x}) - f(x) + g(\hat{x}).u \ , \bar{\varepsilon} = h(\hat{x}) - h(x) \tag{A2}$$

Let us derive the expression for the successive derivatives of the output observation error $\bar{\varepsilon} = \hat{y} - y$ up

to the order n, which yields:

$$\begin{bmatrix} \bar{e}_1 \\ \bar{e}_2 \\ \dot{\bar{e}}_2 \\ \bar{e}_3 \\ \dot{\bar{e}}_3 \\ \ddot{\bar{e}}_3 \end{bmatrix} = \begin{bmatrix} h_1(\hat{x}) - h_1(x) \\ h_2(\hat{x}) - h_2(x) \\ L^1_{f(\hat{x})}h_2(\hat{x}) - L^1_{f(x)}h_2(x) \\ h_3(\hat{x}) - h_3(x) \\ L^1_{f(\hat{x})}h_3(\hat{x}) - L^1_{f(x)}h_3(x) \\ L^2_{f(\hat{x})}h_3(\hat{x}) - L^2_{f(x)}h_3(x) \end{bmatrix}, \begin{bmatrix} \dot{\bar{e}}_1 \\ \ddot{\bar{e}}_2 \\ \bar{e}_3 \end{bmatrix} = \begin{bmatrix} L^1_{f(\hat{x})}h_1(\hat{x}) - L^1_{f(x)}h_1(x) \\ L^2_{f(\hat{x})}h_2(\hat{x}) - L^2_{f(x)}h_2(x) \\ L^3_{f(\hat{x})}h_3(\hat{x}) - L^3_{f(x)}h_3(x) \end{bmatrix} + \begin{bmatrix} v_1 \\ v_2 \\ v_3 \end{bmatrix}. \tag{A3}$$

If $e_x = \hat{x} - x \Rightarrow x = \hat{x} - e_x$, the above equations allow for constructing diffeomorphic mappings [24] in the following:

$$\bar{\varepsilon} = \Phi(e_x, \hat{x}) = \begin{bmatrix} \bar{e}_1 \\ \bar{e}_2 \\ \dot{\bar{e}}_2 \\ \bar{e}_3 \\ \dot{\bar{e}}_3 \\ \ddot{\bar{e}}_3 \end{bmatrix} = \begin{bmatrix} \Phi_{11}(e_x, \hat{x}) \\ \Phi_{21}(e_x, \hat{x}) \\ \Phi_{22}(e_x, \hat{x}) \\ \Phi_{31}(e_x, \hat{x}) \\ \Phi_{32}(e_x, \hat{x}) \\ \Phi_{33}(e_x, \hat{x}) \end{bmatrix} = \begin{bmatrix} h_1(\hat{x}) - h_1(\hat{x} - e_x) \\ h_2(\hat{x}) - h_2(\hat{x} - e_x) \\ L^1_{f(\hat{x})}h_2(\hat{x}) - L^1_{f(\hat{x}-e_x)}h_2(\hat{x} - e_x) \\ h_3(\hat{x}) - h_3(\hat{x} - e_x) \\ L^1_{f(\hat{x})}h_3(\hat{x}) - L^1_{f(x)}h_3(\hat{x} - e_x) \\ L^2_{f(\hat{x})}h_3(\hat{x}) - L^2_{f(x)}h_3(\hat{x} - e_x) \end{bmatrix}. \tag{A4}$$

If $e_x = 0$, then all components of vector $\bar{\varepsilon}$ are identically 0 irrespectively of $\hat{x}$, i.e. $\Phi(0\ ,\ \hat{x}) = 0$. For the details of the proof, see [36]. Lemma 1 is guaranteed provided that the mapping $\Phi(e_x\ ,\ \hat{x})$ is locally bijective in the neighborhood of $e_x = 0$. The bijectivity of the mapping will be defined as $\det J(0, \hat{x}) \neq 0, \forall \hat{x}$ using the Jacobean matrix $J(e_x, \hat{x}) = \frac{\partial(\Phi(e_x\ ,\ \hat{x}))}{\partial e_x}$ [36]. The Jacobean matrix is expressed as:

$$J(e_x, \hat{x}) = \frac{\partial(\Phi(e_x, \hat{x}))}{\partial e_x} = \begin{bmatrix} \partial(\Phi_{11}(e_x, \hat{x}))/\partial e_x \\ \partial(\Phi_{21}(e_x, \hat{x}))/\partial e_x \\ \partial(\Phi_{22}(e_x, \hat{x}))/\partial e_x \\ \partial(\Phi_{31}(e_x, \hat{x}))/\partial e_x \\ \partial(\Phi_{32}(e_x, \hat{x}))/\partial e_x \\ \partial(\Phi_{33}(e_x, \hat{x}))/\partial e_x \end{bmatrix} = \begin{bmatrix} \partial(-h_1(\hat{x} - e_x))/\partial e_x \\ \partial(-h_2(\hat{x} - e_x))/\partial e_x \\ \partial(-L^1_{f(\hat{x}-e_x)}h_2(\hat{x} - e_x))\Big/\partial e_x \\ \partial(-h_3(\hat{x} - e_x))/\partial e_x \\ \partial(-L^1_{f(x)}h_3(\hat{x} - e_x))\Big/\partial e_x \\ \partial(-L^2_{f(x)}h_3(\hat{x} - e_x))\Big/\partial e_x \end{bmatrix}, \tag{A5}$$

$$\frac{\partial(\Phi_{11}(e_x, \hat{x}))}{\partial e_x} = -\frac{\partial(h_1(x))}{\partial x}\frac{\partial(\hat{x} - e_x)}{\partial e_x}. \tag{A6}$$

The replacement of $x = \hat{x} - e_x$ in the above equation, and equating $e_x = 0$ and $\partial(\hat{x} - e_x)/\partial e_x = -1$, yields $J(e_x, \hat{x})|_{e_x=0} = O_{sq}(\hat{x})$. This confirms the nonsingularity of $J(e_x, \hat{x})|_{e_x=0} = O_{sq}(\hat{x})$, as stated in Assumption 1. Therefore, the observer in Eq. (18) with the observability matrix in Eq. (21) reconstructs the state of the system in Eq. (9) in finite time. It is seen that the observer input v_i is selected in such a way that the vector $\bar{\varepsilon}$ is steered to 0 in finite time.

Appendix 2. Sliding variable and its time derivatives

- **Inner loop:**

$$\begin{aligned}
&\dot{S}_2 = \dot{\omega}_{cp} - \dot{\omega}^*_{cp} \Rightarrow \dot{S}_2 = \phi_2(t,x) + \gamma_2(t,x)\ \ v_{cm} \\
&\gamma_2(t,x) = \tfrac{\pi}{30\,J_{cp}}(\eta_{cm}\tfrac{k_t}{J_{cp}R_{cm}}) \\
&\phi_2(t,x) = \tfrac{\pi}{30\,J_{cp}}(-\eta_{cm}\tfrac{k_t}{J_{cp}R_{cm}}k_v x_1 \\
&-(A_0 + A_1x_1 + A_{00} + A_{10}x_1 + A_{20}(x_1)^2 + A_{01}x_2 + A_{11}x_2x_1 + A_{02}(x_2)^2))
\end{aligned} \tag{A7}$$

- **Outer loop:**

$$\begin{aligned}
&\dot{S}_1 = \dot{\lambda}_{O2} - \dot{\lambda}^*_{O2} = \phi_1(t,x) + \gamma_1(t,x)\omega_{cp} \\
&\dot{S}_1 = \dot{\lambda}_{O2} - \dot{\lambda}^*_{O2} = \tfrac{X_{O_2,in}(1+\Omega_{atm})^{-1}\,K_{sm,out}(\dot{x}_2 - \frac{\dot{x}_4}{M_{O2}}\frac{R_{O2}.T_{st}}{Vca} - \frac{\dot{x}_5}{M_{N2}}\frac{R_{N2}T_{st}}{Vca} - P_{v,ca})}{W_{O2,reacted}} \\
&\gamma_1 = \tfrac{X_{O_2,in}}{W_{O2,reacted}}\tfrac{K_{sm,out}B_{01}(T_{atm} - \frac{T_{atm}}{\eta_{cp}})}{1+\Omega_{atm}}
\end{aligned} \tag{A8}$$

The detailed calculation of ϕ_1 is similar to that of ϕ_2. Therefore, the detailed calculation of ϕ_1 is ignored to avoid complexity.

$$\phi_1 = \left[\frac{\partial S_1}{\partial x_1}\ \frac{\partial S_1}{\partial x_2}\ \frac{\partial S_1}{\partial x_3}\ \frac{\partial S_1}{\partial x_4}\ \frac{\partial S_1}{\partial x_5}\ \frac{\partial S_1}{\partial x_6}\right] \times [f(x,t) + g(x,t)\omega_{cp}] \tag{A9}$$

References

[1] Larminie J, Dicks A. Fuel cell systems explained. 2nd ed. New York, NY, USA: Wiley, 2003.

[2] Wang C, Nehrir MH, Shaw SR. Dynamic models and model validation for PEM fuel cells using electrical circuits. IEEE T Energy Convers 2005; 20: 442–451.

[3] Rakhtala SM, Ghaderi R, Ranjbar A, Fadaeian T, Nabavi A. Current stabilization in fuel cell/battery hybrid system using fuzzy-based controller. In: IEEE 2009 Electrical Power & Energy Conference; 22–23 October 2009. Montreal, QC, Canada: IEEE. pp. 1–6.

[4] Pukrushpan J, Peng H, Stefanopoulou A. Simulation and analysis of transient fuel cell system performance based on a dynamic reactant flow model. In: Proceedings of the ASME International Mechanical Engineering Congress & Exposition; 17–22 November 2002. New Orleans, LA, USA: ASME. pp. 1–12.

[5] Pukrushpan J, Stefanopoulou A, Peng H. Control of fuel cell breathing. IEEE Contr Syst Mag 2004; 24: 30–46.

[6] Na W, Gou B, Diong B. Nonlinear control of PEM fuel cells by exact linearization. IEEE T Ind Appl 2007; 43: 1426–1433.

[7] Na W, Gou B. Feedback-linearization-based nonlinear control for PEM fuel cells. IEEE T Energy Convers 2008; 23: 179–190.

[8] Na W, Gou B. Exact linearization based nonlinear control of PEM fuel cells. In: IEEE 2007 Power Engineering Society General Meeting; 24–28 June 2007. Tampa Bay, FL, USA: IEEE. pp. 1–6.

[9] Grujicic M, Chittajallu KM, Pukrushpan J. Control of the transient behaviour of polymer electrolyte membrane fuel cell systems. J Automobile Eng 2004; 218: 1239–1250.

[10] Garcia-Gabin W, Dorado F, Bordons C. Real-time implementation of a sliding mode controller for air supply on a PEM fuel cell. J Process Contr 2010; 20: 325–336.

[11] Kunusch C, Puleston PF, Mayosky MA, Davila A. Sliding mode strategy for PEM fuel cells stacks breathing control using a super-twisting algorithm. IEEE T Control Syst Technol 2009; 17: 167–174.

[12] Kunusch C, Puleston PF, Mayosky MA, Davila A. Advances in HOSM control design and implementation for PEM fuel cell systems. In: 14th IFAC International Conference on Methods and Models in Automation and Robotics; 19–21 August 2009. Miedzyzdroje, Poland: IFAC. pp. 1000–1007.

[13] Kunusch C, Puleston PF, Mayosky MA, Davila A. Efficiency optimization of an experimental PEM fuel cell system via super twisting control. In: 11th International Workshop on Variable Structure Systems; 26–28 June 2010. Mexico City, Mexico: IEEE. pp. 319–324.

[14] Talj R, Hilairet M, Ortega R. Second order sliding mode control of the moto-compressor of a PEM fuel cell air feeding system, with experimental validation. In: 35th Annual Conference of the IEEE Industrial Electronics Society; 3–5 November 2009. Porto, Portugal: IEEE. pp. 2790–2795.

[15] Matraji I, Laghrouche S, Wack M. Cascade control of the moto-compressor of a PEM fuel cell via second order sliding mode. In: 50th IEEE Conference on Decision and Control and European Control Conference; 12–15 December 2011. Orlando, FL, USA: IEEE. pp. 633–638.

[16] Kazmi H, Bhatti AI, Iqbal M. Parameter estimation of PEMFC system with unknown input. In: 11th International Workshop on Variable Structure Systems; 26–28 June 2010. Mexico City, Mexico: IEEE. pp. 301–306.

[17] Kazmi H, Bhatti AI. Parameter estimation of proton exchange membrane fuel cell system using sliding mode observer. Int J Innov Comput Inf Control 2012; 8: 5137–5148.

[18] Kim ES. Observer based nonlinear state feedback control of PEM fuel cell systems. J Electr Eng Technol 2012; 7: 891–897.

[19] M'Sirdi NK, Rabhi A, Fridman L, Davila J, Delanne Y. Second order sliding-mode observer for estimation of vehicle dynamic parameters. Int J Vehicle Des 2008; 48: 190–207.

[20] Pisano A, Salimbeni D, Usai E, Rakhtala SM, Ranjbar A. Observer-based output feedback control of a PEM fuel cell system by high-order sliding mode technique. In: European Control Conference; 17–19 July 2013. Zurich, Switzerland: IEEE. pp. 2495–2500.

[21] Peng H, Pukrushpan J. Control of Fuel Cell Power Systems: Principle, Modeling, Analysis and Feedback Design. Berlin, Germany: Springer-Verlag, 2004.

[22] Kunusch C, Puleston PF, Mayosky MA, Husar AP. Control-oriented modeling and experimental validation of a PEMFC generation system. IEEE T Energy Conver 2011; 28: 851–861.

[23] Kunusch C. Second order sliding mode control of a fuel cell stack using a twisting algorithm. MSc, National University of La Plata, La Plata, Argentina, 2006.

[24] Isidori A. Nonlinear Control Systems. London, UK: Springer-Verlag, 1996.

[25] Levant A. Higher-order sliding modes, differentiation and output-feedback control. Int J Contr 2003; 76: 924–941.

[26] Davila J, Rios H, Fridman L. State observation for nonlinear switched systems using nonhomogeneous high-order sliding mode observers. Asian J Control 2012; 14: 911–923.

[27] Pisano A, Usai E. Sliding mode control: a survey with applications in math. Math Comput Simulat 2011; 81: 954–979.

[28] Levant A. Quasi-continuous high-order sliding-mode controllers. IEEE T Autom Control 2005; 50: 1812–1816.

[29] Levant A. Sliding order and sliding accuracy in sliding mode control. Int J Contr 1993; 58: 1247–1263.

[30] Moreno J, Osorio M. A Lyapunov approach to second-order sliding mode controllers and observers. In: 47th IEEE Conference on Decision and Control (CDC2008); 9–11 December 2008. Cancun, Mexico: IEEE. pp. 2856–2861.

[31] Moreno J. A linear framework for the robust stability analysis of a generalized super-twisting algorithm. In: 6th IEEE International Conference on Electrical Engineering, Computing Science and Automatic Control; 10–13 January 2009. Toluca, Mexico: IEEE. pp. 12–17.

[32] Davila A, Moreno J, Fridman L. Optimal Lyapunov function selection for reaching time estimation of super twisting algorithm. In: 48th IEEE Conference on Decision and Control; 15–18 December 2009. Shanghai, China: IEEE. pp. 8405–8410.

[33] Shtessel YB, Moreno JA, Plestan F, Fridman L, Poznyak AS. Super-twisting adaptive sliding mode control: a Lyapunov design. In: 49th IEEE Conference on Decision and Control; 15–17 December 2010. Atlanta, GA, USA: IEEE. pp. 5109–5113.

[34] Moreno J. A Lyapunov approach to output feedback control using second-order sliding modes. IMA J Math Control Info 2012; 29: 291–308.

[35] Bartolini G, Pisano A, Usai E, Levant A. On the robust stabilization of nonlinear uncertain systems with incomplete state availability. J Dyn Syst Measure Contr 2000; 122: 738–745.

[36] Davila J, Fridman L, Pisano A, Usai E. Finite-time state observation for non-linear uncertain systems via higher-order sliding modes. Int J Contr 2009; 82: 1564–1574.